ACS OMEGA

http://pubs.acs.org/journal/acsodf

Article

Intrinsic Properties of GO/RGO Bilayer Electrodes Dictate Their Inter-/Intralayer Intractability to Modulate Their Capacitance Performance

Tamanna Islam,[§] Md. Mahedi Hasan,[§] Subrata Sarker, and A. J. Saleh Ahammad*

Cite This: *ACS Omega* 2023, 8, 14013−14024

Read Online

ACCESS | Metrics & More | Article Recommendations | Supporting Information

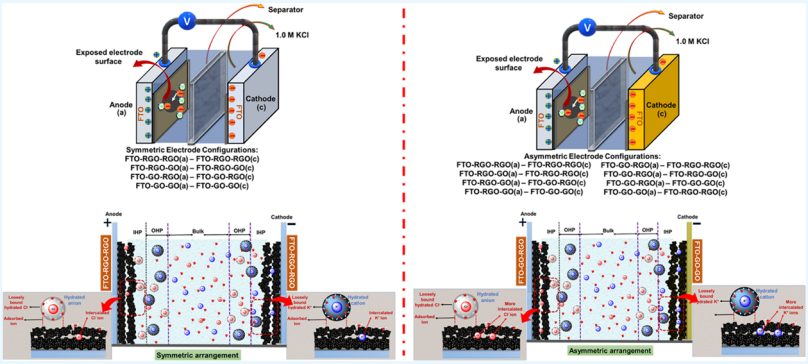

ABSTRACT: The demand for high-capacity energy storage along with high power output and faster charging has made supercapacitors a key area of energy research. The charge storage capacity of capacitors is largely dependent on the electrode materials utilized. To that end, graphene oxide (GO) and reduced GO (RGO) have been extensively employed for preparing supercapacitors. However, to date, no study has reported utilizing a GO/RGO bilayer electrode material for supercapacitor application. Herein, we report the synthesis of GO/RGO bilayer electrodes on fluorine-doped tin oxide (FTO) conducting substrates with four different combinations, namely, RGO-RGO, RGO-GO, GO-RGO, and GO-GO. Electrochemical capacitance analysis based on a symmetrical electrode configuration revealed that FTO-GO-RGO electrodes had the best areal capacitance performance. However, the highest specific areal capacitance (27.85 mF/cm^2) for both symmetric/asymmetric configurations was achieved with FTO-GO-RGO as the anode and FTO-GO-GO as the cathode. The heterogeneous capacitance performance of the GO/RGO bilayer systems was analyzed based on structural characterization and computational simulation methods. Based on our analysis, we identified that inter-/intralayer molecular interaction of the GO/RGO bilayer sheets through the confinement pressure effect might have prompted their unique physicochemical properties. This work highlights the importance of probing multilayer GO/RGO electrode fabrication methods for preparation of high-capacity supercapacitors through fine-tuning their structural and molecular properties.

1. INTRODUCTION

Supercapacitors are the first choice for applications that require high power (>10 kW/kg) in a short burst or fast charge/discharge (<10 s).[1,2] Advances in materials development through extensive investigation of the supercapacitor mechanism have made it possible to use them in electric vehicles, portable electronic devices, and even as biocompatible materials in biomedical devices.[3−5] Unlike commercially available rechargeable batteries, supercapacitor devices function by storing opposite charges at the electrode−electrolyte interface through a physical adsorption process allowing fast charging while longer discharging time desirable for application in integrated energy devices.[6] Based on their working mechanism, supercapacitors can be classified as electrochemical double-layer (EDL)/pseudo/hybrid capacitors.[6] At the same time, depending on the electrode material used, supercapacitors can be classified as symmetric/asymmetric.[6,7] Irrespective of the working mechanism and electrode configuration supercapacitor, electrode materials must have exceptional electrical properties and the ability to store a large amount of charge.

The molecular and structural arrangement of a material determines its electrochemical properties. Graphene deriva-

Received: January 28, 2023
Accepted: March 22, 2023
Published: April 5, 2023

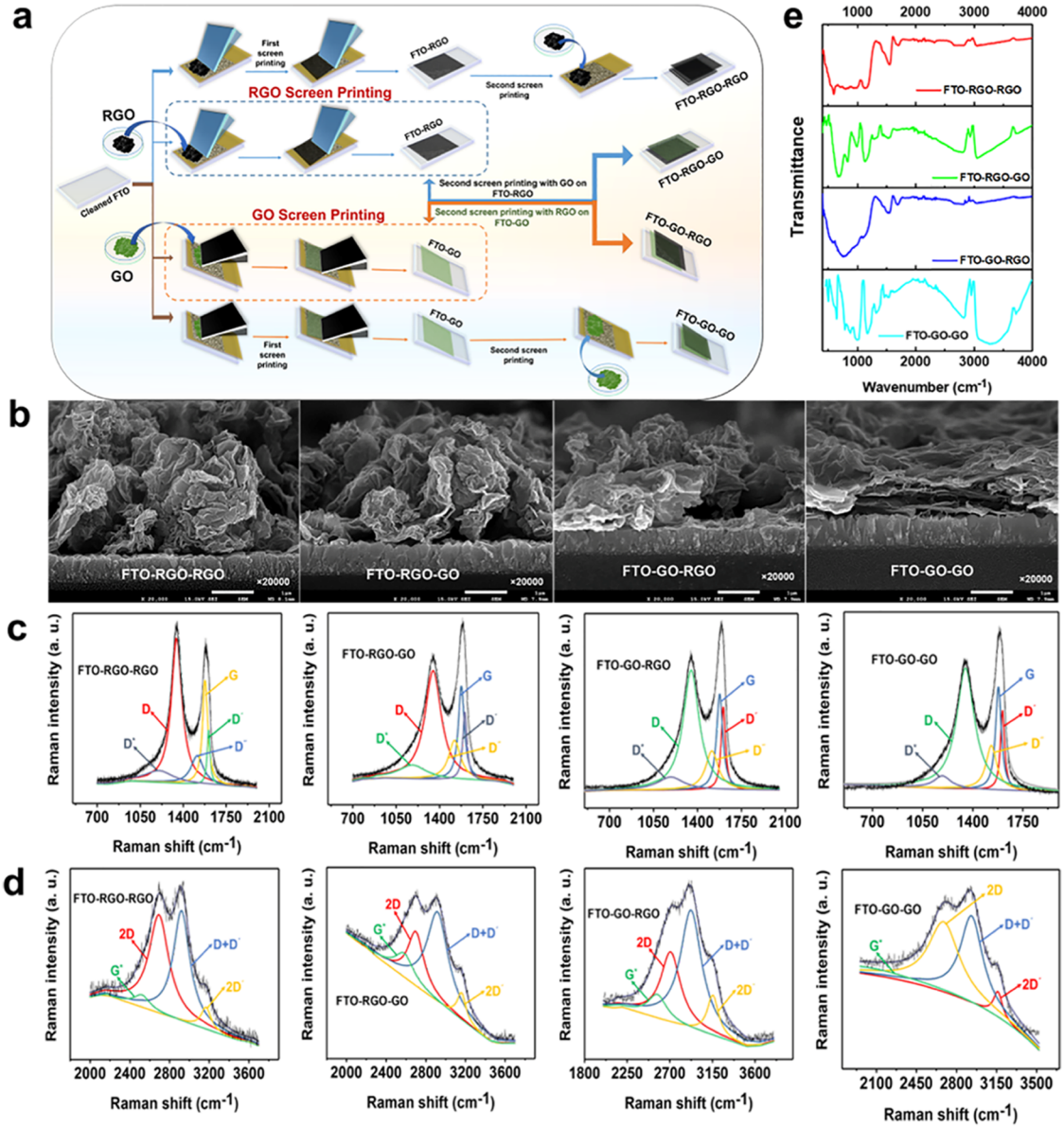

Figure 1. GO/RGO bilayer electrodes retained their individuality. This resulted in unique material properties. Study of morphological, structural, and compositional properties of fabricated RGO-RGO, RGO-GO, GO-RGO, and GO-GO. (a) Schematic illustration of the four different electrode modification processes. (b) Cross-sectional SEM micrographs of four materials (20,000× magnification). (c) and (d) Deconvoluted first- (D/G) and second- (overtone) order Raman spectra of four materials. (e) FT-IR spectra of all materials.

tives are known for their versatile electrochemical properties.[8,9] Structurally, graphene consists of two-dimensional (2D) stacked hexagonal sheets providing an exceptionally wide effective surface area, while chemically engineered layer spacing would allow charged electrolytes to directly interact and intercalate through the structures, rendering improved charge storage ability during the discharging process.[10−12] The functionality of graphene oxide (GO) and reduced GO (RGO) in supercapacitor applications is also well studied.[10,13] Furthermore, high mechanical strength and compatibility of GO and RGO sheets make them appealing for constructing high-performance flexible supercapacitor devices.[14,15] While GO offers high specific surface area, increased functional group, and good conductivity, it suffers from drawbacks like quick aggregation due to strong plane-to-plane pi−pi interaction and small pore size that hinders its ability to interact with electrolytes.[16] RGOs, on the other hand, have larger pores due to the defects that arise during reduction of GO and are less likely to aggregate while maintaining exceptional electrical properties.[17,18] Hence, in most cases, doping various kinds of substrates, including metal, organic/inorganic ligands, and polymers, with GO and RGO materials has extensively been used in fabricating high-capacitance supercapacitors.[19] These approaches were able to successfully induce more layer integrity in graphene materials; however, to date, no study has reported the capacitance properties of the GO/RGO bilayer electrode system. Traditionally, mixing GO and RGO fails to provide any significant improvement of the capacitance property.[20] As these materials have similar physicochemical properties when taken in a suitable solvent, GO and RGO tend to interact with each other in a random fashion, losing their independent properties.[20−22] This is the case even when stabilizers are used to prevent layer aggregation

https://doi.org/10.1021/acsomega.3c00573
ACS Omega 2023, 8, 14013−14024

as these stabilizers are incapable of directing GO/RGO toward directional interaction.[21]

Theoretically, microporosity in structures offers confinement effect for guest atoms/molecules to intercalate and bind in the host materials.[23,24] It is because the confinement effect results in partial pressure in the porous structure to exhibit unique features that improve the electronic and intrinsic properties of the material.[25] This behavior of materials can be observed in cases of gas molecule confinement in polymers, metal−organic frameworks, etc.[23,25] Such confined pressure effects are also attainable in stacked layers of graphene 2D sheets to obtain improved layer integrity. Usually, GO, due to the presence of an excess number of oxygen functionalities, including hydroxyl, epoxy, and carbonyl groups, shows better structural unity and layer-to-layer distance.[22,25] Upon thermal annealing, most of the functionalities disappear, lowering the separation between layers in RGO.[26] Therefore, by controlling the annealing temperature, the quantity of functional groups on the graphene sheets can be constrained to a specific value necessary for maintaining specific interlayer spacing. Herein, we propose a simple layer-by-layer screen-printing method that ensured the individuality of the GO and RGO layer while allowing interlayer interaction among these materials. The screen-printing method has been used for preparing GO-RGO and RGO-GO electrodes on the fluorine-doped tin oxide (FTO) base substrate. We have also prepared GO-GO and RGO-RGO electrodes and compared them with the GO-RGO and RGO-GO electrodes. The once-prepared electrodes were sintered at 450 °C after fabrication, resulting in GO/RGO sheets with specific interlayer spacing that allowed charge storing via interlayer intercalation and physical adsorption for supercapacitor application. Raman, cross-sectional scanning electron microscopy (SEM), and Fourier-transformed infrared (FT-IR) techniques have been utilized in determining the structural properties of the GO/RGO bilayer electrodes. Cyclic voltammetry (CV) and galvanostatic charge−discharge (GCD) techniques were used for analyzing the capacitance properties. Density functional theory (DFT) and molecular dynamic (MD) simulations were used to analyze the molecular properties of the prepared GO/RGO bilayer systems. Analysis of experimental and computational results revealed that interlayer and intralayer interaction among GO and RGO functional groups gives rise to unique physicochemical properties that are responsible for the disparate capacitance properties of the GO/RGO bilayer electrodes.

2. EXPERIMENTAL SECTION

2.1. GO and RGO Syntheses. GO and RGO materials were synthesized following the modified Hummer's method and the hydrazine reduction process, respectively, which has been described in our previous reports.[17,27] Initially, graphite flakes (Sigma-Aldrich, Germany) were oxidized to form GO. This was done following the modified Hummer's method. In this process, for each gram of graphite flake, 40 mL of H_2SO_4 was taken together. The mixture was kept on an ice bath in a round-bottom flask. Once the solution cooled down sufficiently, 3.5 g of $KMnO_4$ was mixed for each gram of graphite flake and mixed completely through stirring for about 2 h. Once the $KMnO_4$ was mixed completely, 150 mL of water was added to the solution using a glass cylinder. In this final mixture, H_2O_2 was added in a dropwise manner using a 1 mL micropipette, observing the bubble formation due to the oxidation process. After filtering the solution, the residue was collected and dried in a vacuum oven for two days. The dried mass was collected as GO. This GO was used for further experiments relating to screen-printing and RGO synthesis.

The synthesized GO from the modified Hummer's method was reduced to get the RGO. After collection, GO was initially dispersed in water in a round-bottom flask. With continuous stirring at 80 °C, 1 μL of hydrazine was added to the aqueous solution for 3 mg of GO. The solution turned to black color with the addition of hydrazine, indicating the completion of the reduction process. The RGO material was also vacuum-dried for two days after filtration before use for any further experiment.

2.2. GO/RGO Paste Preparation. The as-synthesized GO and RGO were used for making pastes that could be screen-printed. The same amounts of GO (0.05 g) and ethyl cellulose (0.05 g) were mixed in 10 mL of ethanol in a 50 mL round-bottom flask with continuous stirring. When the substances were completely dissolved, 1 mL of terpinol was added to the solution with vigorous stirring. The final solution was dried in a vacuum oven to obtain the final GO paste. The same procedure was followed for the preparation of RGO paste.

2.3. GO/RGO Bilayer Electrode Preparation. The prepared GO/RGO pastes were used for preparing the screen-printed electrodes. FTO glass substrates (Pilkington TEC8, 8 Ω/square) were used as base connectors due to their excellent conductivity. The electrodes were prepared through sequential screen-printing of each layer of GO/RGO paste to form the bilayer GO/RGO electrodes (Figure 1a). Initially, the GO/RGO paste was taken on a mesh screen that had a 1 cm × 1 cm area with 50 μm pore size. Using this mesh screen, the first layer of GO/RGO was printed on the FTO glass substrate. The glass substrates were sonicated and thoroughly rinsed with deionized water before screen-printing. Once a layer of GO or RGO paste was screen-printed, the electrodes were then dried at 110 °C on a hotplate to ensure proper binding with the electrodes. This process was repeated a second time to get the final FTO-RGO-RGO, FTO-RGO-GO, FRO-GO-GO, and FTO-GO-RGO electrodes. Finally, the electrodes were sintered at 450 °C in an argon atmosphere to remove any organic materials without oxidizing the carbon materials. The electrodes are named based on substrates to the final layer. Thus, for the FTO-GO-RGO electrode, the GO layer was deposited on the FTO substrate and then the RGO layer was deposited on the GO-layered FTO substrate.

2.4. Surface Characterization. The Raman spectra were obtained using LabRAM HR Evolution instrument from HORIBA Scientific. The excitation energy wavelength (λ_l) was 514 nm. Crystallite size (L_a) was determined following eq 1.

$$L_a = (2.4 \times 10^{-10})\lambda_l^4 \left(\frac{I_D}{I_G}\right)^{-1} \quad (1)$$

I_D and I_G stand for intensities of D and G bands, respectively.

FT-IR spectroscopy was used for analyzing the surface functional groups for the GO/RGO bilayer electrodes (VERTEX 80v, Bruker). Cross-sectional SEM and a thickness profiler were used for analyzing the thickness of the deposited GO/RGO layers. Cross-sectional SEMs were obtained with an E-SEM (FEI Quanta 400 FEG), and an α-step, Dektak 150 (Veeco), thickness profiler was used for directly measuring the thickness.

https://doi.org/10.1021/acsomega.3c00573
ACS Omega 2023, 8, 14013−14024

2.5. Capacitance Measurement. Throughout the electrochemical experiments, 1.0 M KCl was used as the supporting electrolyte. All CV and GCD experiments were performed with the KCl supporting electrolyte containing aqueous solutions and repeated at least three times with individual electrodes to ensure the reproducibility of the experimental results. The CHI 660E was used for performing all electrochemical experiments. The operating potential window (OPW) was determined using CV and GCD techniques. For OPW determination, a CV scan rate of 50 mV/s and a GCD current density of 2 mA/cm^2 were utilized. The CV scan rate variation was studied from 5 to 500 mV/s to study the CV shape change and the effect of adsorption/diffusion processes on the total capacitance. GCD analyses at different current densities from 2 to 50 mA/cm^2 were done to see the change in discharge time and curve shape.

The areal specific capacitance (C_A) measurements from CV and GCD were done following eqs 2 and 3.

$$C_A = \int_{V_1}^{V_2} I(V)\mathrm{d}V/\Delta V \frac{\mathrm{d}V}{\mathrm{d}t}A \tag{2}$$

$$C_A = I_d t_d/\frac{\mathrm{d}V}{\mathrm{d}t}A \tag{3}$$

Here, $\int_{V1}^{V2} I(V)\mathrm{d}V$ is the integrated area for forward and reverse sweep from CV, ΔV is the potential in volts, $\mathrm{d}V/\mathrm{d}t$ is the scan rate (V/s), I_d is the discharge current mA, t_d is the discharge time for the specific discharge current, and A is the area in cm^2.

The surface adsorption capacitance and diffusion intercalation capacitance contribution to the total capacitance were determined using Dunn's method (eq 4) and the power law relationship or the Cottrell equation (eq 5).

$$I(V) = k_1\left(\frac{\mathrm{d}V}{\mathrm{d}t}\right) + k_2\left(\frac{\mathrm{d}V}{\mathrm{d}t}\right)^{1/2} \tag{4}$$

$$I = a\frac{\mathrm{d}V^b}{\mathrm{d}t} \tag{5}$$

Here, $I(V)$ is the current at a constant voltage, $k_1(\mathrm{d}V/\mathrm{d}t)$ and $k_2(\mathrm{d}V/\mathrm{d}t)^{1/2}$ are the contributions from surface adsorption and diffusion intercalation capacitance, respectively, and a and b are constant parameters that are adjustable. The values of b, k_1, and k_2 were measured through analyzing the CV data for potential 0.005−0.05 V/s scan rates.

2.6. Computational Methodology. The GO and RGO structures were prepared so that the oxygen contents were around 25 and 18%. The structures were prepared based on the results from Raman and FT-IR analyses. Density functional theory (DFT) analyses were performed to determine the molecular properties of the RGO-RGO, RGO-GO, GO-RGO, and GO-GO electrode systems. The molecular properties of the electrode systems were further compared with GO and RGO electrode systems. The interlayer and intralayer interaction properties were analyzed through electron density distribution analysis. The bulk properties were analyzed with molecular dynamic (MD) simulations. Analysis of MD simulation revealed how the GO/RGO bilayers interacted with H_2O, H^+, OH^-, K^+, and Cl^- ions. Energy change and intercalation of the charged species into the GO/RGO systems were studied with the MD simulation.

The GO and RGO structures were put in a vacuum slab system with 30 Å periodic boundary. The slabs were prepared with 2 × 2 supercell periodicity. Generalized gradient approximation and revised Perdew−Burke−Ernzerhof functionals were utilized to study the exchange correlation. To accurately represent the contribution from core electrons while minimizing the computational simulation time, DFT Semi-core Pseudopots were utilized. A double numerical polarization basis set was used for treating electronic properties along with the COSMO solvent system. Tolerance was set for 1×10^{-5} for the self-consistent field.

The MD simulation was carried out using condensed-phase-optimized molecular potentials for an atomistic simulation studies-II forcefield. Adsorption location, energy change, and structural relationship analysis were performed following MD simulation results. For all energy, force, and displacement analyses, an ultrafine parameter was utilized.

3. RESULTS

3.1. Screen-Printing GO/RGO Bilayer Gives Rise to Unique Structural Properties. Initially, an equal amount of synthesized GO and RGO materials through the modified Hammer's method and the chemical reduction process was double screen-printed on an FTO electrode to obtain FTO-RGO-RGO, FTO-RGO-GO, FTO-GO-RGO, and FTO-GO-GO electrodes.[17,27] The overall process of electrode preparation for each of the electrodes is schematically represented in Figure 1a. Once the electrodes were dried after sintering at 450 °C, we performed characteristic SEM analysis to study the morphological properties of the modified FTO electrodes. Figure 1b shows the characteristic cross-sectional SEM micrographs of the modified electrodes. The sheets of individual layers can be seen from the magnified SEM images, indicating that the GO/RGO sheets did not completely coalesce together and instead maintained their individuality. Interestingly, we observed that the thickness of the double-printed GO/RGO materials on FTO exhibited significant variations even though equal amounts of GO and RGO materials were initially taken for screen-printing followed by sintering at a constant temperature. Figure S1a−d shows how the layer thickness changed for different electrode systems. The electrode material thickness varied in the order FTO-RGO-RGO (4.23 μm) < FTO-RGO-GO (2.85 μm) < FTO-GO-RGO (4.68 μm) < FTO-GO-GO (4.158 μm). The confined pressure effect resulting from stacking of GO/RGO could be the reason for this difference in overall height of the electrode material.[25] These observations clearly indicated that the GO/RGO material tended to retain their distinct structural features after electrode preparation, which was important for exhibiting different charge storage properties during supercapacitor applications.

Owing to differences in the molecular structures of the synthesized carbon materials (GO-GO, GO-RGO, RGO-GO, and RGO-RGO), the characteristic intrinsic properties including crystallinity, sp^2 carbon orders in the ring, total oxygen content, degree of disorder, etc. may vary. We have investigated the variation of such properties of all four materials by employing Raman spectroscopy. This technique is suitable for analyzing defects/disorder in the structure of various carbon materials based on different spectral parameters obtained through deconvoluting well-defined spectral bands/peaks at a specific wavenumber.[28] Figure S1e shows the Raman spectra of FTO, FTO-GO-GO, FTO-GO-RGO, FTO-RGO-GO, and FTO-RGO-RGO, at a wide frequency range (800−4000 cm^{-1}), which resulted in first and second orders of Raman bands, namely, D/G and overtone bands. The D band

https://doi.org/10.1021/acsomega.3c00573
ACS Omega 2023, 8, 14013−14024

represents the breathing mode of vibration of the sp^2 ring with A_{1g} symmetry, which arises from the in-plane one-phonon vibrational process of the hexagonal ring. The D band typically results from a high degree of disorder in graphene, where the ring is typically adjacent to defects or edge planes. While on the other hand, the G band corresponds to the stretching mode of vibration of the sp^2 ring with A_{2g} symmetry and is the primary band observed in graphite and graphene. Initially, no significant differences were observed in D and G band positions, and in all cases, the bands were centered at 1351 and 1580 cm^{-1}, respectively. However, considering the widening and superposition of spectral bands, Raman band intensity ratio (I_D/I_G) analysis often provides ambiguous information about crystal order and defects in carbon materials.[28] For this reason, we have employed the Lorentzian method for deconvoluting all sets of Raman peaks. Deconvolution of first-order Raman D and G bands resulted in five fitted curves within the 1000−1800 cm^{-1} spectral range, which are D*, D″, D′, D, and G. The D* band at 1183−1190 cm^{-1} is generally known to result from disordered graphitic lattices with the sp^3 orbital or the sp^3-rich phase, nanocrystalline diamond, hexagonal diamond, and trans polyacetylene in the lattice boundaries.[26,28] The D″ band corresponds to the amorphous phase of the material, originates in the 1516−1531 cm^{-1} spectral range, and is inversely proportional to the crystallinity.[26] The D′ represents defect-associated features centered at 1607−1610 cm^{-1} and shows intravalley resonance with the G band.[29] Figure 1c shows the first-order deconvoluted Raman spectra of all four materials. Different spectral band parameters including peak position (X_p), full width at half-maximum (FWHM), and peak area in percentage (A) are summarized in Table S1.

The relative spectroscopic study of all four materials exhibits notable changes in peak intensities and positions due to double screen-printing of either the same or different materials on the FTO electrode and resulted in structural alterations with multilayer stacking and additional hybridization (sp^2 and sp^3), defects, etc. in the electrode system. The level of degree of graphitization can be estimated from the intensity ratio of D and G bands. Generally, the I_D/I_G ratio exhibits two behaviors with increasing disorder in graphene materials.[30] I_D/I_G increases at a region of low defect density due to elastic scattering resulting from lattice defects. In the high defect density region, I_D/I_G begins to decrease as increasing amorphous phases in the carbon structure would lower all Raman modes. The values of the I_D/I_G ratio were obtained to be 1.17, 1.25, 1.16, and 1.39 for GO-GO, GO-RGO, RGO-GO, and RGO, respectively, indicating that the defect density could vary from high to medium in the structure with RGO-RGO having the lowest defect density compared to the other three materials (Table S2). This also demonstrates that RGO-RGO might have a nanocrystalline structure with relatively small grain boundaries. The amount of sp^3 carbon can also be derived from the G peak position and the I_D/I_G ratio based on the amorphization trajectory proposed by Ferrari et al.[31] According to this trajectory, the estimated percentages of sp^3 carbon were derived to be approximately ∼9, 12, 13, and 6%, respectively, for GO-GO, GO-RGO, RGO-GO, and RGO-RGO materials (Table S2).

Although the I_D/I_G ratio provides much important information on the degree of deformation, sp^2/sp^3 cluster sizes, and edge/grain boundaries, it is not sufficient to evaluate details of the degree of reduction and the amount of oxygen content in the material due to overlapping and broadening of D and G bands. The value of the area ratio and intensity ratio of D*, D′, and D″ bands to the G band was significantly lower compared to the I_D/I_G ratio (Tables S3 and S4). It has been reported that the intensity of D* and D″ bands normalized to the G band correlates very well with the amount of oxygen content and hence the degree of reduction in the synthesized RGO structure.[26,32] López-Díaz et al. reported that the value of I_{D*}/I_G reached ∼0.15 for up to 20−22% of the oxygen content in GO and decreased to around 0.1 when annealed at 600 °C temperature, at which most of the oxygen functionalities were removed from the GO structure.[26] In this study, the estimated I_{D*}/I_G ratio varied from 0.11 (RGO-RGO) to 0.15 (RGO-GO), indicating the lowest amount of oxygen content (∼17−18%) in RGO-RGO and the highest oxygen content (∼20−22%) in the RGO-GO material. The D′ band is related to the defect concentration in the structure and is proportional to the number of vacancies and sp^3 hybridization.[26] Therefore, the presence of sp^3 hybridized carbon might be responsible for the D′ band.

The second-order Raman bands were deconvoluted using Lorentzian functions into four curves, namely, 2D, D + D′, 2D′, and G* bands. Different spectral parameters including peak position (X_p), full width at half-maximum (FWHM), and peak area in percentage (A) are summarized in Table S5. The deconvoluted spectra of all four materials are represented in Figure 1d. To further validate our assessment of second-order overtone bands, we plotted the frequency of 2D, D + D′, and 2D′ bands of the second-order spectral region against twice the frequency of the D band, the sum of the frequency of D and D′ bands, and twice the frequency of the D′ band, respectively. As can be seen from the Figure S1f, the spectral peak position of second-order bands matched well with the first-order bands, indicating that these bands are undoubtedly 2D, D + D′, and 2D′. 2D and 2D′ bands result from two phonons of opposite wave functions, where the Raman selection rule is satisfied. Usually, these bands originate even in the absence of defects; however, the D + D′ band requires defects in the structure and originates from phonons with different wave vectors. 2D is known to correlate with the number of layers in graphene-based materials and their order in the structural moiety.[30] The number of layers can be estimated from the intensity ratio of I_{2D}/I_G and can vary depending on the shape and center of gravity of the peak. In single-layer graphene materials, the 2D band would result in a single Lorentzian curve with an FWHM of 24 cm^{-1}, whereas in the multilayer structure, this band would split into multiple bands.[33] However, in rotationally random multilayer graphene, the 2D band results in a single peak with a wider FWHM and shifted the peak position due to the absence of interlayer interactions between stacked layers.[30,34] The center of gravity of the 2D Raman band of our materials shifted from 2691 (GO-GO) to 2711 (GO-RGO) and 2694 (RGO-RGO) to 2701 (GO-RGO) cm^{-1}. In an ideal case, the 2D band appears approximately at ∼2690 cm^{-1} in single-layer pristine graphene. These observations indicate that the materials with a combination of GO and RGO printed at the electrode had randomly oriented stacked layers, while screen-printing of similar materials (GO-GO and RGO-RGO) resulted in a lesser number of randomly oriented sheets. In all cases, the printed electrode had multilayer GO and RGO structures.

FT-IR spectroscopy was used for determining the functional group interactions in the GO/RGO systems (Figure 1e). All

https://doi.org/10.1021/acsomega.3c00573
ACS Omega 2023, 8, 14013−14024

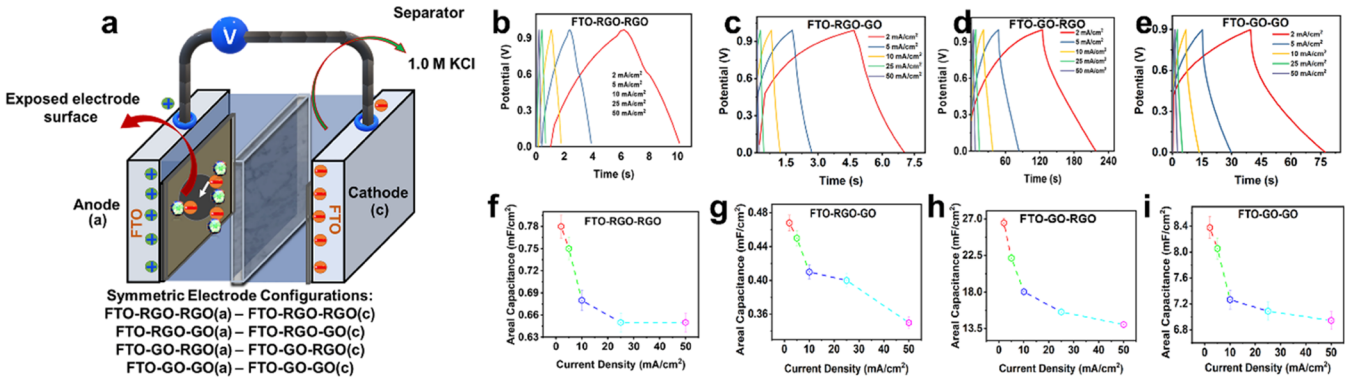

Figure 2. Symmetric electrode arrangement shows disparate capacitance property for GO/RGO bilayer electrodes. (a) Schematic representation of electrode arrangement for the symmetric configurations. (b–e) Galvanostatic charge–discharge (GCD) curves of four symmetric systems with electrodes, namely, FTO-RGO-RGO, FTO-RGO-GO, FTO-GO-RGO, and FTO-GO-GO. The current densities used in different GCDs are 2, 5, 10, 25, and 50 mA/cm^2. (f–i) Plot of areal specific capacitance vs current density of four symmetric systems. The value of areal capacitance was obtained from GCD analysis.

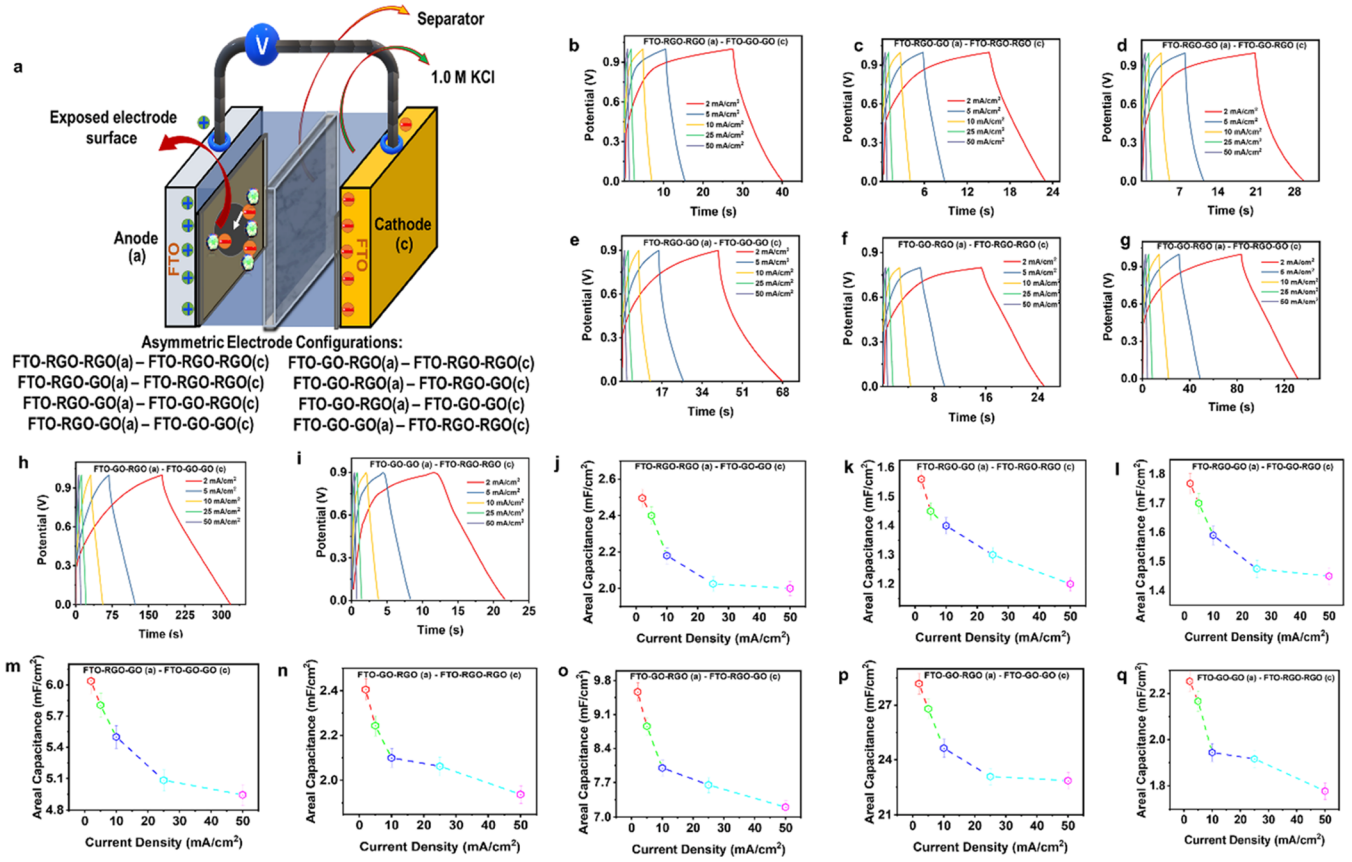

Figure 3. Asymmetric anode/cathode arrangements profoundly influence the charge–discharge processes. (a) Scheme showing electrode arrangements for the asymmetric electrode configuration. Eight different orientations of electrodes as anode (a) and cathode (c) were utilized, which are, (1) FTO-RGO-RGO as the anode and FTO-GO-GO as the cathode, (2) FTO-RGO-GO as the anode and FTO-RGO-RGO as the cathode, (3) FTO-RGO-GO as the anode and FTO-GO-RGO as the cathode, (4) FTO-RGO-GO as the anode and FTO-GO-GO as the cathode, (5) FTO-GO-RGO as the anode and FTO-RGO-RGO as the cathode, (6) FTO-GO-RGO as the anode and FTO-RGO-GO as the cathode, (7) FTO-GO-RGO as the anode and FTO-GO-GO as the cathode, and (8) FTO-GO-GO as the anode and FTO-RGO-RGO as the cathode. (b–i) GCD curves obtained from all asymmetric systems with current density being utilized are 2, 5, 10, 25, and 50 mA/cm^2. (j–q) Plots of areal capacitance vs current density of eight asymmetric systems. The value of areal capacitance was obtained from GCD analysis.

systems showed common ring deformation (~838 cm^{-1}), C–OH stretching and bending (~990 cm^{-1}), and stretching of symmetric –OH bonding (−3400 cm^{-1}) absorption bands.[35] These GO/RGO systems also showed bands for H-bonding in their absorption spectrum, showing that there were both intralayer and interlayer interactions between the GO/RGO systems. The FTO-GO-GO system had the highest absorption band near ~990 cm^{-1}.[19] This is expected as GO contains a relatively high number of functional groups in its structure. It is likely that the presence of such functional groups would allow

https://doi.org/10.1021/acsomega.3c00573
ACS Omega 2023, 8, 14013–14024

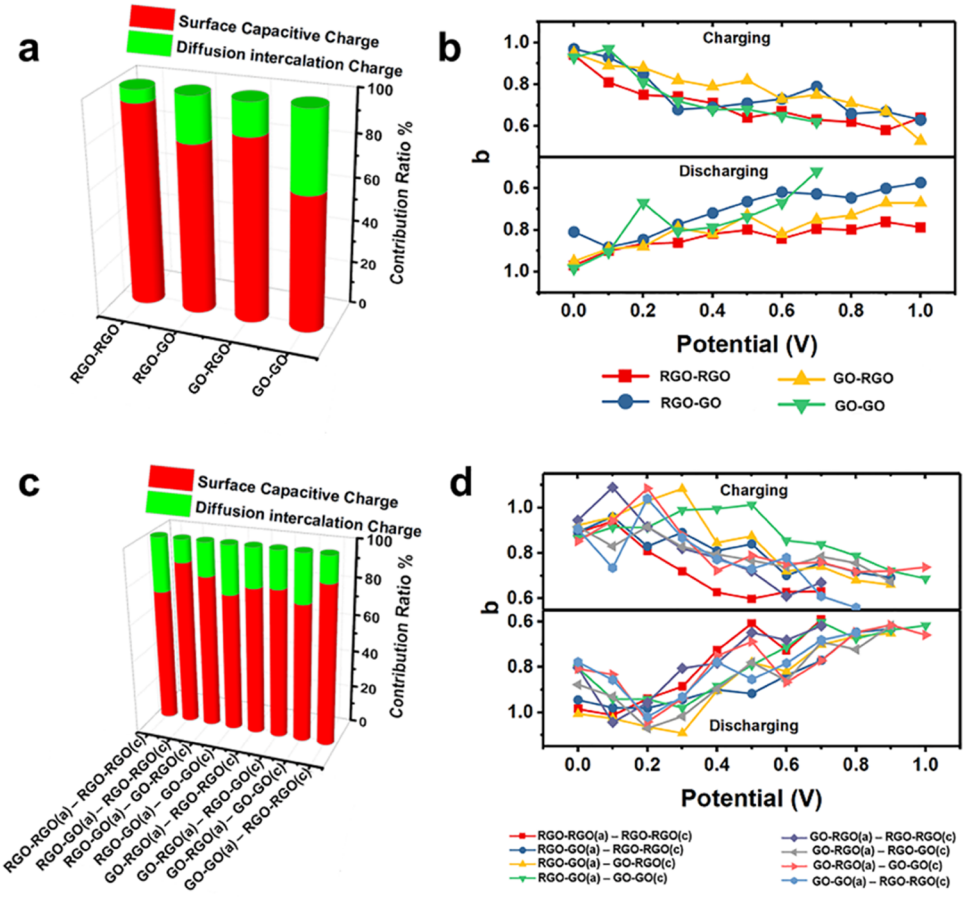

Figure 4. Total capacitance resulting from capacitive and faradic charge transfer processes. (a) and (c) show the percentage of electrical double-layer and faradic capacitance resulting in a CV obtained at 5 mV/s scan rate for symmetric and asymmetric electrode systems, respectively. (b) and (d) represent the changes of the *b* value obtained from Dunn's method and the power law relationship with respect to the CV potential (V) for symmetric and asymmetric electrode systems.

for increased wettability of the SC electrode surface and promote increased diffusion of ionic species through the porous structure.

3.2. Capacitance of GO/RGO Bilayer Electrodes Changes Depending on Electrode Setup Configuration. The atypical surface characterization results for the GO/RGO electrodes motivated us to test their performance in energy storage. The electrochemical cells were prepared to test both symmetric and asymmetric configurations of the GO/RGO electrodes (Figures 2 and 3). The electrodes were covered with nonconducting tape, exposing only a 0.07 cm^2 surface that would interact with the 1.0 M KCl solution. The choice of electrolyte is important during supercapacitor fabrication. While acidic H_2SO_4 and alkaline KOH are known to show very good conductivity and overall capacitance performance, the highly acidic/alkaline solutions can damage the electrodes over long periods of use.[33] The neutral aqueous supporting electrolyte was chosen for the electrochemical experiments because KCl has high conductivity and does not damage the electrode over time.[37] This allowed us to determine the areal specific capacitance for all electrodes. Cyclic voltammetry (CV) and galvanostatic charge−discharge (GCD) operations for symmetric configuration in a two-electrode setup revealed disparate behavior in charge storage (Figures S2 and S3). The RGO-RGO electrode had a box-shaped CV from 0.0 to 0.6 V, and beyond that, it had a quasi-rectangular shape. However, for the RGO-GO, GO-RGO, and GO-GO electrodes, a quasi-rectangular shape could be observed throughout the CV scanning window (Figure S2). The GO-RGO electrodes maintained the quasi-rectangular shape over the widest operating potential window (OPW) and the highest capacitance value in CV analysis (Figure S2c). The current signal abruptly changed after 1.0 V for each electrode. GCD operations for the symmetric electrode configuration yielded similar results, with GO-RGO having the highest capacitance out of the four electrode systems (Figure S3). The RGO-RGO electrode had the shortest discharge. The CVs of the symmetrical electrode configuration retained their quasi-rectangular shape until almost 250 mV/s scan rate, indicating that up to this scan rate the charging/discharging process was regulated through the double-layer capacitance process (Figure S4). At higher scan rates, there was a sudden increase in current density for all four GO/RGO systems. The sudden rise in current density is an indicator of the faradic charge transfer contribution to the overall capacitance.[36] The GCD cycles reflected that at lower current densities, there was a slight IR drop for the GO-RGO and GO-GO systems, while the RGO-RGO and RGO-GO systems had a steady discharge current signal (Figure 2). For the symmetrical GO/RGO electrode configurations, the GO-RGO system performed best as it had the highest areal specific capacitance (17.85 mF/cm^2 at 1.0 V); however, the RGO-RGO system showed the most ideal

https://doi.org/10.1021/acsomega.3c00573
ACS Omega 2023, 8, 14013−14024

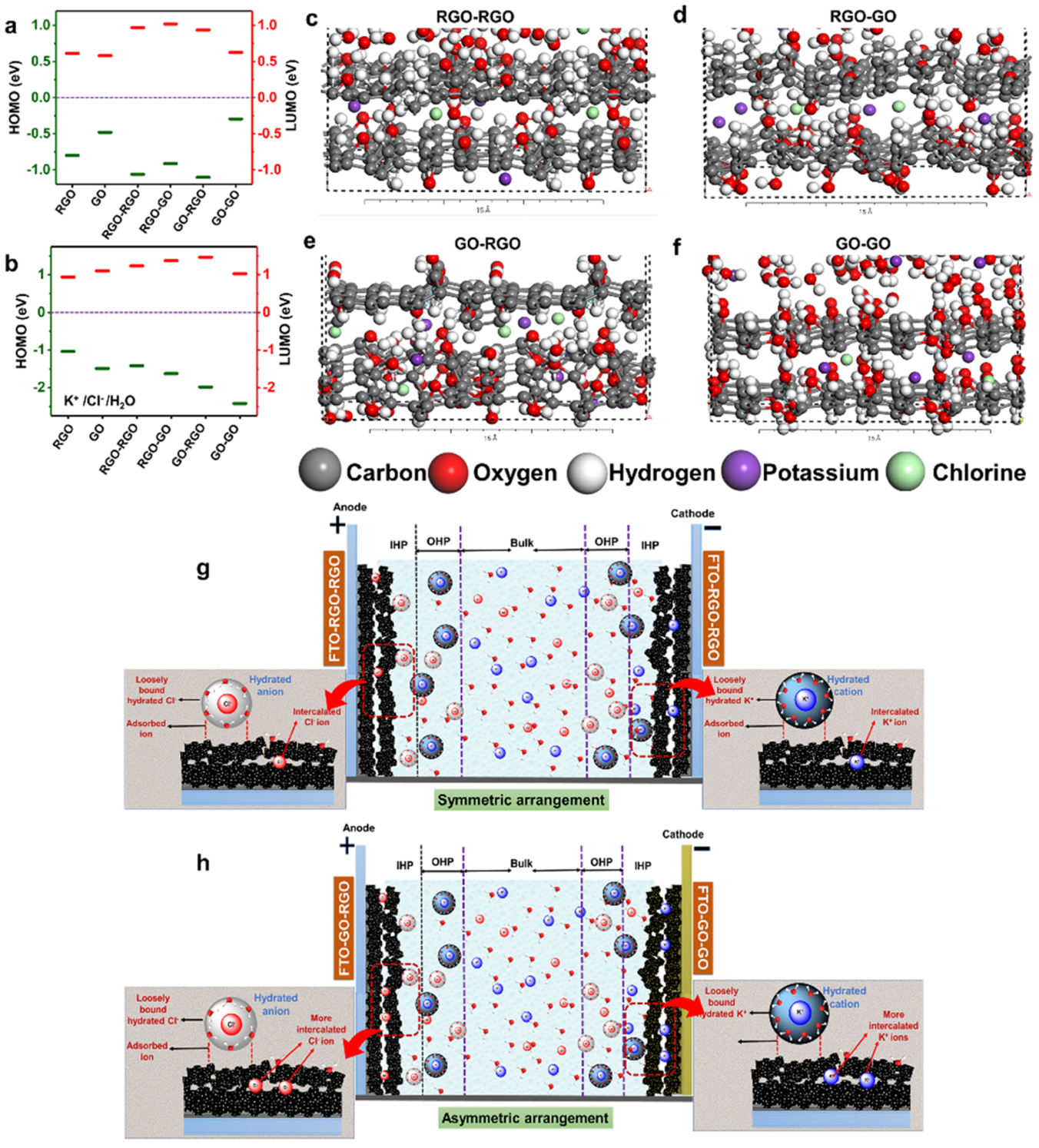

Figure 5. Inter-/intralayer molecular interactions give rise to unique properties of GO/RGO bilayer electrodes. (a) HOMO−LUMO molecular orbitals for the DFT optimized structures of RGO, GO, RGO-RGO, RGO-GO, GO-RGO, and GO-GO simulations. (b) HOMO−LUMO molecular orbitals for the DFT optimized structures of RGO, GO, RGO-RGO, RGO-GO, GO-RGO, and GO-GO simulations in the COSMO solvation system with K^+ and Cl^+ ions. (c−f) Intercalation of K^+/Cl^+ ions in the lowest energy configurations of RGO-RGO, RGO-GO, GO-RGO, and GO-GO systems from MD simulation. Structural and molecular properties of the GO/RGO bilayer system influences their inter-/intralayer interactions. (g) Symmetric and (h) asymmetric configuration of the electrode arrangement influences how they interact with hydrated cations and anions at the interfacial layer and regulates their diffusion-controlled intercalation.

behavior for electrochemical double-layer capacitance (EDLC). It is likely that while the RGO-RGO system worked as an ideal EDLC, the other systems had pseudo-capacitance contribution due to faradic charge transfer processes.

For the asymmetric electrode configurations, the electrodes were prepared in the same way as for symmetrical configurations (Figure 3). The electrodes were arranged in eight different configurations for testing their performance as

https://doi.org/10.1021/acsomega.3c00573
ACS Omega 2023, 8, 14013−14024

anodes/cathodes in the asymmetrical electrochemical setup. The asymmetrical SC configurations retained an ideal box shape for EDLC only up to 0.5 V in CV analysis (Figure S5). Beyond 0.5 V, these configurations showed a quasi-reversible CV plot. Higher areal specific capacitance values were obtained for configurations with GO-RGO(a) as anodes, while lower areal specific capacitance values were obtained for configurations with RGO-GO(a) as anodes (Figure S6). GCD plots for asymmetric SC configurations also showed the longest discharge time for the GO-RGO(a)-GO-GO(c) configuration along with the highest capacitance (Figures S7 and S8). Scan rate variation analysis for the asymmetric configurations revealed that these electrodes had a stable quasi-rectangular shape until only 100 mV/s, and beyond that, they had a sharp increase in the current value (Figure S9). The capacitance value decreased with increasing scan rate (Figure S10). The diffusion rate limiting effect might have decreased the faradic charge storage process, resulting in decreased capacitance. The GCD discharge curve at lower charge densities declined steadily, while at higher charge densities, the discharge current dropped at a much faster rate (Figure 3). The fast decline in discharge could be due to the internal resistance of electrode materials that resulted in a greater IR drop.[38] The notable change in capacitance value with charge density variation from 2 to 50 mA/cm^2 indicated that both EDLC and pseudo-capacitance contributions changed with increasing charge density for the asymmetric configurations.

To determine the contributions from the faradic charge transfer process to the overall capacitance, we utilized Dunn's method and the power law relationships (eqs 4 and 5).[39,40] CV analysis of the symmetrical systems revealed that for RGO-RGO the surface capacitive charge contribution was nearly 94% (Figures 4a and S11). Increase in the diffusion intercalation charge percentage to the total capacitance followed the trend RGO-RGO (6%) < GO-RGO (15%) < RGO-GO (21%) < GO-GO (37%). The slope from the power law relationship ($\log i$ vs $\log \nu$) yielded the b value for the symmetrical systems (Figures 4b and S12). A b value close to 0.5 indicates pseudocapacitive contribution of the diffusion-controlled faradic charge transfer process, while a b value close to 1.0 indicates a diffusion-independent charging process. For RGO-RGO electrodes, the b value was close to 0.9 from 0.0 to 0.4 V; the value was close to 0.7 for the potentials after that. The RGO-GO electrodes showed a b value around 0.6 from 0.3 to 1.0 V. For RGO-GO electrodes, the b value was around 0.8 up to 0.4 V and around 0.6 V after that potential. For GO-GO electrodes, the b value changed to around 0.6 from 0.2 V and continued decreasing. The changes in b values for the symmetrical system show that RGO-RGO electrodes had the most contribution from the surface capacitive charge at each potential during the CV scanning, while GO-GO electrodes had the most contribution from the diffusion intercalation.

Analyzing the CVs for asymmetric electrode configurations with Dunn's method allowed us to separate the contribution from double-layer capacitance to a diffusion-controlled process (Figures 4c and S13). The results for diffusion intercalation contribution to the total capacitance varied significantly depending on the anode/cathode configuration. The contribution from diffusion intercalation was very high for all electrode configurations (>20%). This high diffusion intercalation likely contributed to the greater capacitance value for the asymmetrical configurations compared to the symmetrical configurations. A general trend that emerged from the analysis is, whenever the GO-GO(c) electrode was used as the cathode there was greater contribution from diffusion intercalation in the total capacitance. The power law relationship for the asymmetric configurations had almost similar trends of b value change for eight configurations (Figures 4d and S14). The b value remained close to 1.0 up to 0.4 V, and then, the b values were close to around 0.6/0.7 for almost the rest of the CV scanning area.

Dunn's equations and power law analyses confirmed that EDLC and pseudo-capacitance contributions were part of the total capacitance for all electrode configurations. Analysis for the symmetric configurations showed that the capacitive/diffusion contribution varied significantly for each electrode system. Analysis of the asymmetric configurations further showed that these electrodes could contribute to the total capacitance depending on their individual characteristics. Physicochemical properties of the GO/RGO systems could be the key factor modulating their electrochemical behavior.

3.3. Molecular Properties Influence Inter-/Intralayer Interactions of GO/RGO Sheets. As from CV and GCD analyses, the trend of the charge storage capacity showed significant variation depending on the way symmetric/asymmetric electrochemical cells were constructed and the use of different combinations of screen-printed GO/RGO materials. Both EDLC and faradic capacitance contributed to the total capacitance in a rather disparate manner that was independent and unique for each of the electrode configurations. Owing to significant structural distinctions, electronic orientation, and compositional variation, a discrete double-layer pattern and charge intercalation properties emerged during charging/discharging processes in symmetric/asymmetric electrode configurations. This conclusion inspired us to investigate the inter-/intralayer interactions between GO/RGO sheets and, consequently, hydrated K^+ and Cl^- ions that could possibly show competitive interacting affinity toward different electrode systems using computational approaches. Initially, the vibrational frequency-based infrared spectra for the simulated spectra were compared with the infrared spectra for the prepared electrodes (Figure S15). The infrared spectra for the simulated GO/RGO systems were comparable to the screen-printed GO/RGO electrodes. Figure 5a represents the electronic structure in terms of the highest occupied molecular orbital (HOMO) and the lowest unoccupied molecular orbital (LUMO) of the single GO/RGO material and the double-layer RGO-RGO, RGO-GO, GO-RGO, and GO-GO materials, indicating doubly screen-printed electrodes. The energy gaps between HOMO and LUMO were observed to be significantly high in RGO-RGO, RGO-GO, and GO-RGO compared to their individual identity. This finding indicates that layer-by-layer printing of GO and RGO should result in rather stable configurations. When hydrated K^+ and Cl^- were incorporated in the system, the energy gap between HOMO and LUMO exceeded 1.5 eV, which was relatively high compared to the system with no hydrated ions.[41] The HOMO−LUMO energy gap was also found to be significantly large in all four composite materials, demonstrating that the HOMO and LUMO further reoriented themselves throughout the structure in the presence of hydrated ions in such a way that it minimized the energy required to enable stable electronic structures.

MD simulation results show that both K^+ and Cl^+ ions could intercalate through the upper layer of GO/RGO and enter the inner layer of the GO/RGO electrodes (Figure 5c−f). For MD

https://doi.org/10.1021/acsomega.3c00573
ACS Omega 2023, 8, 14013−14024

simulations, ten K^+ and Cl^- were studied to see their intractability with the GO/RGO bilayer electrodes. GO-RGO (4 K^+, 4 Cl^-) electrodes had the greatest number of ions that intercalated to the inner layer, followed by RGO-GO (4 K^+, 2 Cl^-), GO-GO (3 K^+, 2 Cl^-), and RGO-RGO (2 K^+, 2 Cl^-). The desorption energy values for K^+ and Cl^- ions were similar for all electrode configurations (Table S7). The adsorption energy was the most negative for the GO-RGO system and the least negative for the RGO-RGO and GO-GO systems. The adsorption energy values indicated that the KCl aqueous system interacted with the GO-RGO and RGO-GO systems most deliberately. However, OH^- had the least negative interaction energy in all systems. This result indicated that solvent interaction was a key contributor for all four electrode systems.

4. DISCUSSION

The capacitance process of GO/RGO bilayer FTO electrodes involves both surficial and internal interactions. As potential is applied to the anode and cathode, the cations and anions start accumulating in the oppositely charged electrode surfaces. Based on electrochemical theories, these approaching ions form the inner Helmholtz plane (IHP) and the second layer is formed with oppositely charged ions (OHPs) (Figure 5g,h). Once at the surface, the ions of IHP can enter the electrode through pores of appropriate sizes.[36] Electrode surface wettability due to the hydrophilic functional groups is also known to play an important part in modulating ion intractability.[42] When these ions enter the pores and do not undergo any electrochemical reaction, this results in ideal EDLC. However, the total capacitance of GO/RGO electrodes had a significant contribution from faradic charge transfer. Hence, in these electrodes, there was reversible charge transfer. This charge transfer could have been due to the hydrated shell of the cations and anions instead of the direct oxidation/reduction of K^+ and Cl^-. The highly negative (~23 kJ/mol) energy related to the OH^- adsorption is an indicator of this phenomenon. The interlayer spacing of GO/RGO bilayer systems likely modulated their capability to accommodate K^+ and Cl^- ions as we saw from the MD simulation that different numbers of cations and anions could intercalate in the internal structure. However, without in situ XPS analysis, with potential scanning, this cannot be confirmed with just computational simulation analysis.

The discharge time for the symmetric systems followed the trend GO-RGO > GO-GO ≥ RGO-GO and RGO-RGO (Figure 5g). However, for the asymmetric system, the trend was GO-RGO(a)-GO-GO(c) > GO-RGO(a)-RGO-GO(c) > RGO-GO(a)-GO-GO(c) > GO-RGO(a)-RGO-RGO(c) > GO-GO(a)-RGO-RGO(c) > RGO-RGO(a)-GO-GO(c) > RGO-GO(a)-GO-RGO(c) > RGO-GO(a)-RGO-RGO(c) (Figure 5h). The asymmetric GO-RGO(a)-GO-GO(c) configuration had the longest discharging time, almost twice that of the symmetric GO-RGO system. On the other hand, RGO-GO(a)-GO-RGO(c) had the second lowest discharge time. The eight asymmetric configurations make it clear that the GO-GO electrode performed the best when utilized as a cathode and the GO-RGO electrode performed the best when used as an anode. Sintering the GO and RGO pastes together at 450 °C might have reoriented their structure in such a way that allowed for effective inter-/intralayer interaction. While the confined pressure effect might have resulted in separation of the GO/RGO sheets enough to allow cations and anions to intercalate, the functional groups present on these GO/RGO sheets might have interacted with the hydrated ions for the oxidation/reduction process. Thus, even though hydration of K^+ and Cl^- ions affected their ability to reach the electrode surface, it was likely the inter-/intralayer interaction among the GO/RGO sheets gave rise to the unique molecular properties that modulated that areal capacitance.

Despite using multiple characterization techniques and computational simulation methods, there are some big areas that we could not explore. For instance, Raman analysis revealed that the GO and RGO materials had a multilayer arrangement in the prepared GO/RGO bilayer electrodes, but the number of layers in the synthesized GO/RGO materials and how much the confined pressure effect was at work in those layers were not studied. Cross-sectional SEM and FT-IR gave information regarding GO/RGO sheet arrangement and surficial functional groups, but the actual structural properties of the inner layers of the bilayer GO/RGO were not investigated through any characterization method. Understanding the role of the solvation effect of ions would also greatly benefit in determining the capacitance process mechanism in a more wholistic manner. Another key area of investigation would be trying to determine the faradic/non-faradic contribution from individual electrodes in the asymmetric arrangement of GO/RGO bilayer electrodes. Our analysis revealed the faradic/non-faradic contribution in the charge storage process for the overall system, and the charge storage capacity for the symmetric/asymmetric configurations was so disparate that comparing them would not yield a sound analysis. Hence, finding ways to investigate and overcome these limitations would result in significant improvement of the capacitance properties of not just GO/RGO but 2D materials in large. In future, we aim to study structural changes, plane-to-plane confinement processes, and interlayer spacing between GO and RGO bilayer through in situ XPS, X-ray diffraction (XRD), and thermogravimetric analysis during capacitance analysis electrochemical experiments. We also envision to explore different synthetic approaches to obtain single and few-layer graphene materials for supercapacitor applications.

5. CONCLUSIONS

Herein, we reported the fabrication of GO/RGO bilayer electrodes through the screen-printing technique that ensured GO and RGO retained their individual properties while allowing them to interact with each other. Cross-sectional SEM indicated that GO/RGO sheets retained their individuality through the confined pressure effect. Raman and FT-IR analyses showed that each of the RGO-RGO, RGO-GO, GO-RGO, and GO-GO electrodes had their own characteristic properties. CV and GCD analyses confirmed their disparate electrochemical behavior and capacitance properties. Analysis of CV data showed that capacitance for these electrodes was dependent on both EDLC and faradic charge transfer processes. DFT simulation results showed that the HOMO−LUMO energy levels changed depending on the GO/RGO assembly and influenced the interaction of the K^+ and Cl^- electrolytes with the electrodes. However, MD simulations revealed that it is likely that hydration of K^+ and Cl^- electrolytes influenced their ability to interact with the electrodes. Our analysis pointed out that inter/intralayer interactions of GO/RGO sheets due to their functional groups regulated their ability to interact with ions from solvent, charge

https://doi.org/10.1021/acsomega.3c00573
ACS Omega 2023, 8, 14013−14024

storage mechanism, and even the OPW for a given solvent. As the FTO-GO-RGO(a) and FTO-GO-GO(c) arrangement of electrodes had the highest areal specific capacitance, it clearly shows the benefit of using bilayer GO/RGO electrodes in the fabrication of high-performance capacitors. Further research in preparation of multilayer GO/RGO electrodes would allow overcoming the limitations discussed in this work, greatly advancing the 2D material-based supercapacitor application.

■ ASSOCIATED CONTENT

Supporting Information

The Supporting Information is available free of charge at https://pubs.acs.org/doi/10.1021/acsomega.3c00573.

Spectral position (X_p), full width at half-maximum (FWHM), and areal percentage (A %) of deconvoluted first-order Raman spectral bands (D*, D, D″, G, and D′ bands); sp^3 percentage and crystallite size L_a; intensity ratios for D*, D, G, and D′ bands; area ratios for D*, D, G, and D′ bands; spectral position (X_p), full width at half-maximum (FWHM), and areal percentage (A %) of deconvoluted second-order Raman spectral bands (G*, 2D, D + D′, and 2D′ bands); assignment of FT-IR spectra for FTO-GO-GO, FTO-GO-RGO, FTO-RGO-GO, and FTO-RGO-RGO electrodes; energy changes in kJ/mol for each molecule from MD simulations; cross-sectional SEM micrographs of FTO-RGO-RGO, FTO-RGO-GO, FTO-GO-RGO, and FTO-GO-GO materials with layer thickness (10,000× magnification); full Raman spectra of FTO, FTO-RGO-RGO, FTO-RGO-GO, FTO-GO-RGO, and FTO-GO-GO electrodes obtained at a wide spectral range from 100 to 4000 cm^{-1}; CV behaviors obtained at different potential windows for different symmetric electrode systems; GCD plots obtained for different potential windows for all four symmetric electrode systems, areal capacitance obtained from GCD analysis vs the operating potential window, and GCD plots obtained at 5 mA/cm^2 current density; CV plots obtained at different scan rates from 5 to 500 mV/s for four symmetric and eight asymmetric electrode systems; variation of areal capacitance with respect to the applied scan rates for all four symmetric systems; CV behaviors obtained at different potential windows for eight different asymmetric electrode systems; GCD plots obtained for different potential windows for all asymmetric electrode systems; plot of areal capacitance obtained from GCD analysis vs the operating potential window; variation of areal capacitance with respect to the applied scan rates for eight asymmetric systems; determination of k_1 and k_2 parameters using Dun's method; plot of $i/v^{1/2}$ vs $v^{1/2}$ for all four symmetric systems; determination of the b parameter using the Cottrell relation; plot of $\log i$ vs $\log v$ for all symmetric and asymmetric systems; determination of k_1 and k_2 parameters using Dun's method; plot of $i/v^{1/2}$ vs $v^{1/2}$ for all asymmetric systems; determination of the b parameter using the Cottrell relation; and simulated vibrational mode (infrared) spectra for FTO-RGO-RGO, FTO-RGO-GO, FTO-GO-RGO, and FTO-GO-GO (PDF)

■ AUTHOR INFORMATION

Corresponding Author

A. J. Saleh Ahammad − *Department of Chemistry, Jagannath University, Dhaka 1100, Bangladesh;* orcid.org/0000-0001-7568-5268; Phone: +880 2 223353794; Email: ajsahammad@chem.jnu.ac.bd; Fax: +880 2 7113713

Authors

Tamanna Islam − *Department of Chemistry, Jagannath University, Dhaka 1100, Bangladesh;* Present Address: Environmental Science & Engineering Program, University of Texas at El Paso, El Paso, Texas 79968, United States; orcid.org/0000-0001-9067-4372

Md. Mahedi Hasan − *Department of Chemistry, Jagannath University, Dhaka 1100, Bangladesh;* Present Address: Environmental Science & Engineering Program, University of Texas at El Paso, El Paso, Texas 79968, United States; orcid.org/0000-0001-7683-4544

Subrata Sarker − *University of Skill Enrichment and Technology, Narayanganj 1430, Bangladesh;* orcid.org/0000-0003-4795-2298

Complete contact information is available at: https://pubs.acs.org/10.1021/acsomega.3c00573

Author Contributions

[§]T.I. and M.M.H. contributed equally to this work.

Notes

The authors declare no competing financial interest.

■ ACKNOWLEDGMENTS

This work was supported by The World Academy of Sciences (TWAS) research grant program (20-126 RG/CHE/AS_I-FR3240314137).

■ REFERENCES

(1) Wang, X.; Salari, M.; Jiang, D.; Chapman Varela, J.; Anasori, B.; Wesolowski, D. J.; Dai, S.; Grinstaff, M. W.; Gogotsi, Y. Electrode Material−Ionic Liquid Coupling for Electrochemical Energy Storage. *Nat. Rev. Mater.* **2020**, *5*, 787−808.

(2) Li, Z.; Wang, X.; Zhao, L.; Chi, F.; Gao, C.; Wang, Y.; Yan, M.; Zhou, Q.; Zhao, M.; Wang, X.; Wang, J.; Yuan, M.; Wu, M.; Wang, L.; Zhao, Y.; Qu, L. Aqueous Hybrid Electrochemical Capacitors with Ultra-High Energy Density Approaching for Thousand-Volts Alternating Current Line Filtering. *Nat. Commun.* **2022**, *13*, No. 1309.

(3) Shi, J.; Xu, B.; Shen, Y.; Wu, J. Energy Management Strategy for Battery/Supercapacitor Hybrid Electric City Bus Based on Driving Pattern Recognition. *Energy* **2022**, *243*, No. 122752.

(4) Qi, D.; Liu, Y.; Liu, Z.; Zhang, L.; Chen, X. Design of Architectures and Materials in In-Plane Micro-Supercapacitors: Current Status and Future Challenges. *Adv. Mater.* **2017**, *29*, No. 1602802.

(5) Zhu, S.; Li, Y.; Zhu, H.; Ni, J.; Li, Y. Pencil-Drawing Skin-Mountable Micro-Supercapacitors. *Small* **2019**, *15*, No. 1804037.

(6) Hasan, M. M.; Islam, T.; Shah, S. S.; Awal, A.; Aziz, M. A.; Ahammad, A. J. S. Recent Advances in Carbon and Metal Based Supramolecular Technology for Supercapacitor Applications. *Chem. Rec.* **2022**, *22*, No. 1858072.

(7) Afif, A.; Rahman, S. M.; Tasfiah Azad, A.; Zaini, J.; Islam, M. A.; Azad, A. K. Advanced Materials and Technologies for Hybrid Supercapacitors for Energy Storage—A Review. *J. Energy Storage* **2019**, *25*, No. 100852.

(8) Iqbal, M. F.; Yousef, A. K. M.; Hassan, A.; Hussain, S.; Ashiq, M. N.; Mahmood-Ul-Hassan; Razaq, A. Significantly Improved Electrochemical Characteristics of Nickel Sulfide Nanoplates Using

https://doi.org/10.1021/acsomega.3c00573
ACS Omega 2023, 8, 14013−14024

Graphene Oxide Thin Film for Supercapacitor Applications. *J. Energy Storage* **2021**, *33*, No. 102091.
(9) Wang, Y.; Shi, Z.; Huang, Y.; Ma, Y.; Wang, C.; Chen, M.; Chen, Y. Supercapacitor Devices Based on Graphene Materials. *J. Phys. Chem. C* **2009**, *113*, 13103−13107.
(10) Li, Z.; Gadipelli, S.; Yang, Y.; He, G.; Guo, J.; Li, J.; Lu, Y.; Howard, C. A.; Brett, D. J. L.; Parkin, I. P.; Li, F.; Guo, Z. Exceptional Supercapacitor Performance from Optimized Oxidation of Graphene-Oxide. *Energy Storage Mater.* **2019**, *17*, 12−21.
(11) Wang, Q.; Wang, S.; Guo, X.; Ruan, L.; Wei, N.; Ma, Y.; Li, J.; Wang, M.; Li, W.; Zeng, W. MXene-Reduced Graphene Oxide Aerogel for Aqueous Zinc-Ion Hybrid Supercapacitor with Ultralong Cycle Life. *Adv. Electron. Mater.* **2019**, *5*, No. 1900537.
(12) Liu, C.; Yu, Z.; Neff, D.; Zhamu, A.; Jang, B. Z. Graphene-Based Supercapacitor with an Ultrahigh Energy Density. *Nano Lett.* **2010**, *10*, 4863−4868.
(13) Askari, M. B.; Salarizadeh, P.; Seifi, M.; Ramezan zadeh, M. H.; Di Bartolomeo, A. ZnFe2O4 Nanorods on Reduced Graphene Oxide as Advanced Supercapacitor Electrodes. *J. Alloys Compd.* **2021**, *860*, No. 158497.
(14) Lee, S. P.; Ali, G. A. M.; Hegazy, H. H.; Lim, H. N.; Chong, K. F. Optimizing Reduced Graphene Oxide Aerogel for a Supercapacitor. *Energy Fuels* **2021**, *35*, 4559−4569.
(15) Benzigar, M. R.; Dasireddy, V. D. B. C.; Guan, X.; Wu, T.; Liu, G. Advances on Emerging Materials for Flexible Supercapacitors: Current Trends and Beyond. *Adv. Funct. Mater.* **2020**, *30*, No. 2002993.
(16) Yu, W.; Sisi, L.; Haiyan, Y.; Jie, L. Progress in the Functional Modification of Graphene/Graphene Oxide: A Review. *RSC Adv.* **2020**, *10*, 15328−15345.
(17) Sarker, S.; Lee, K. S.; Seo, H. W.; Jin, Y. K.; Kim, D. M. Reduced Graphene Oxide for Pt-Free Counter Electrodes of Dye-Sensitized Solar Cells. *Sol. Energy* **2017**, *158*, 42−48.
(18) Wei, M.; Qiao, L.; Zhang, H.; Karakalos, S.; Ma, K.; Fu, Z.; Swihart, M. T.; Wu, G. Engineering Reduced Graphene Oxides with Enhanced Electrochemical Properties through Multiple-Step Reductions. *Electrochim. Acta* **2017**, *258*, 735−743.
(19) Malik, M. T. U.; Sarker, A.; Mahmud Rahat, S. M. S.; Shuchi, S. B. Performance Enhancement of Graphene/GO/RGO Based Supercapacitors: A Comparative Review. *Mater. Today Commun.* **2021**, *28*, No. 102685.
(20) Guo, W.; Van Le, Q.; Hasani, A.; Lee, T. H.; Jang, H. W.; Luo, Z.; Kim, S. Y. MoSe2-GO/RGO Composite Catalyst for Hydrogen Evolution Reaction. *Polymers* **2018**, *10*, No. 1309.
(21) Kaushal, A.; Dhawan, S. K.; Singh, V. Determination of Crystallite Size, Number of Graphene Layers and Defect Density of Graphene Oxide (GO) and Reduced Graphene Oxide (RGO). *AIP Conf. Proc.* **2019**, *2115*, No. 030106.
(22) Oliveira, A. E. F.; Braga, G. B.; Tarley, C. R. T.; Pereira, A. C. Thermally Reduced Graphene Oxide: Synthesis, Studies and Characterization. *J. Mater. Sci.* **2018**, *53*, 12005−12015.
(23) Purkait, T.; Singh, G.; Kumar, D.; Singh, M.; Dey, R. S. High-Performance Flexible Supercapacitors Based on Electrochemically Tailored Three-Dimensional Reduced Graphene Oxide Networks. *Sci. Rep.* **2018**, *8*, No. 5799.
(24) Wei, G.; Zhao, X.; Du, K.; Wang, Z.; Liu, M.; Zhang, S.; Wang, S.; Zhang, J.; An, C. A General Approach to 3D Porous CQDs/MxOy (M = Co, Ni) for Remarkable Performance Hybrid Supercapacitors. *Chem. Eng. J.* **2017**, *326*, 58−67.
(25) Sekimoto, Y.; Ohtani, R.; Nakamura, M.; Koinuma, M.; Lindoy, L. F.; Hayami, S. Tuneable Pressure Effects in Graphene Oxide Layers. *Sci. Rep.* **2017**, *7*, No. 1374.
(26) López-Díaz, D.; López Holgado, M.; García-Fierro, J. L.; Velázquez, M. M. Evolution of the Raman Spectrum with the Chemical Composition of Graphene Oxide. *J. Phys. Chem. C* **2017**, *121*, 20489−20497.
(27) Ahammad, A. J. S.; Islam, T.; Hasan, M. M.; Mozumder, M. N. I.; Karim, R.; Odhikari, N.; Pal, P. R.; Sarker, S.; Kim, D. M. Reduced Graphene Oxide Screen-Printed FTO as Highly Sensitive Electrodes for Simultaneous Determination of Dopamine and Uric Acid. *J. Electrochem. Soc.* **2018**, *165*, B174−B183.
(28) Lee, A. Y.; Yang, K.; Anh, N. D.; Park, C.; Lee, S. M.; Lee, T. G.; Jeong, M. S. Raman Study of D* Band in Graphene Oxide and Its Correlation with Reduction. *Appl. Surf. Sci.* **2021**, *536*, No. 147990.
(29) Ferrari, A. C.; Meyer, J. C.; Scardaci, V.; Casiraghi, C.; Lazzeri, M.; Mauri, F.; Piscanec, S.; Jiang, D.; Novoselov, K. S.; Roth, S.; Geim, A. K. Raman Spectrum of Graphene and Graphene Layers. *Phys. Rev. Lett.* **2006**, *97*, No. 187401.
(30) Childres, I.; Jauregui, L. A.; Park, W.; Caoa, H.; Chena, Y. P. Raman Spectroscopy of Graphene and Related Materials. *New Dev. Phot. Mater. Res.* **2013**, 403−418.
(31) Ferrari, A. C.; Robertson, J. Interpretation of Raman Spectra of Disordered and Amorphous Carbon. *Phys. Rev. B* **2000**, *61*, 14095−14107.
(32) Claramunt, S.; Varea, A.; López-Díaz, D.; Velázquez, M. M.; Cornet, A.; Cirera, A. The Importance of Interbands on the Interpretation of the Raman Spectrum of Graphene Oxide. *J. Phys. Chem. C* **2015**, *119*, 10123−10129.
(33) Malard, L. M.; Pimenta, M. A.; Dresselhaus, G.; Dresselhaus, M. S. Raman Spectroscopy in Graphene. *Phys. Rep.* **2009**, *473*, 51−87.
(34) Martín-García, B.; Velázquez, M. M.; Rossella, F.; Bellani, V.; Diez, E.; García Fierro, J. L.; Pérez-Hernández, J. A.; Hernández-Toro, J.; Claramunt, S.; Cirera, A. Functionalization of Reduced Graphite Oxide Sheets with a Zwitterionic Surfactant. *ChemPhysChem* **2012**, *13*, 3682−3690.
(35) Surekha, G.; Krishnaiah, K. V.; Ravi, N.; Padma Suvarna, R. FTIR, Raman and XRD Analysis of Graphene Oxide Films Prepared by Modified Hummers Method. *J. Phys.: Conf. Ser.* **2020**, *1495*, No. 012012.
(36) Islam, T.; Hasan, M. M.; Shah, S. S.; Karim, M. R.; Al-Mubaddel, F. S.; Zahir, M. H.; Dar, M. A.; Hossain, M. D.; Aziz, M. A.; Ahammad, A. J. S. High Yield Activated Porous Coal Carbon Nanosheets from Boropukuria Coal Mine as Supercapacitor Material: Investigation of the Charge Storing Mechanism at the Interfacial Region. *J. Energy Storage* **2020**, *32*, No. 101908.
(37) Pal, B.; Yang, S.; Ramesh, S.; Thangadurai, V.; Jose, R. Electrolyte Selection for Supercapacitive Devices: A Critical Review. *Nanoscale Adv.* **2019**, *1*, 3807−3835.
(38) Anantharaj, S.; Noda, S. IR Drop Correction in Electrocatalysis: Everything One Needs to Know! *J. Mater. Chem. A* **2022**, *10*, 9348−9354.
(39) Gao, F.; Jiangying, Q.; Zongbin, Z.; Quan, Z.; Beibei, L.; Jieshan, Q. A Green Strategy for the Synthesis of Graphene Supported Mn3O4 Nanocomposites from Graphitized Coal and Their Supercapacitor Application. *Carbon* **2014**, *80*, 640−650.
(40) Chao, D.; Zhu, C.; Yang, P.; Xia, X.; Liu, J.; Wang, J.; Fan, X.; Savilov, S. V.; Lin, J.; Fan, H. J.; Shen, Z. X. Array of Nanosheets Render Ultrafast and High-Capacity Na-Ion Storage by Tunable Pseudocapacitance. *Nat. Commun.* **2016**, *7*, No. 12122.
(41) Seenithurai, S.; Pandyan, R. K.; Kumar, S. V.; Mahendran, M. Electronic Properties of Boron and Nitrogen Doped Graphene. *Nano Hybrids* **2013**, *5*, 65−83.
(42) Zhang, J.; Jin, L.; Cheng, J.; Hu, H. Hierarchical Porous Carbons Prepared from Direct Coal Liquefaction Residue and Coal for Supercapacitor Electrodes. *Carbon* **2013**, *55*, 221−232.

https://doi.org/10.1021/acsomega.3c00573
ACS Omega 2023, 8, 14013−14024